Metastable Sodium closo-Hydroborates for Low Temperature All-Solid-State Battery with Thick Cathode

Jin An Sam Oh,[1,2,†] Zihan Yu,[1,†] Chen-Jui Huang,[3] Phillip Ridley,[1] Alex Liu,[1] Tianren Zhang,[4] Bing Joe Hwang,[5,6] Kent J. Griffith,[4,*] Shyue Ping Ong,[1,7,*] Ying Shirley Meng[1,3,7,*]

[1]Aiiso Yufeng Li Family Department of NanoEngineering, University of California San Diego, La Jolla, CA 92093, United States.

[2]Institute of Materials Research and Engineering (IMRE), Agency for Science, Technology and Research (A*STAR), Singapore 138634, Singapore

[3]Pritzker School of Molecular Engineering, The University of Chicago, Chicago, IL 60637, United States

[4]Department of Chemistry, University of California San Diego, La Jolla, CA 92093, United States.

[5]NanoElectrochemistry Laboratory, Department of Chemical Engineering and Sustainable Electrochemical Energy Development Center, National Taiwan University of Science and Technology, Taipei City 106, Taiwan

[6]National Synchrotron Radiation Research Center, Hsinchu 30076, Taiwan

[7]Energy Storage Research Alliance, Argonne National Laboratory, Lamont, IL 60637, United States.

[†]These authors contributed equally to this work.

***Corresponding authors. Email:** k3griffith@ucsd.edu **(KJG);** ongsp@ucsd.edu **(SPO);** shirleymeng@uchicago.edu **(YSM).**

Abstract

All-solid-state batteries featuring a thick cathode layer paired with a high-capacity alloy anode offer enhanced energy density[1,2] and reliable performance, even at subzero temperatures, can outperform their liquid-based counterparts. Enabling such technology requires a solid electrolyte with high ionic conductivity, mechanical formability, and excellent electrochemical stability[3]. While non-close-packed frameworks offer lower symmetry and irregular coordination between mobile ions and anions due to distortion, resulting in higher ionic conductivity[4,5], fast ionic diffusion in hydroborate chemistry is often associated with close-packed or cubic anion frameworks[6-9]. Here, we demonstrate that a metastable, non-close-packed orthorhombic $Na_3(B_{12}H_{12})(BH_4)$ phase possesses superionic conductivity of 4.6 mS cm^{-1} at 30 °C, three orders of magnitude improvement over its precursors, alongside excellent reduction stability. High-throughput molecular dynamic simulations reveal that the propensity for anion motion significantly enhances the population of highly mobile Na^+ without affecting the activation energy. By leveraging its high conductivity across a wide temperature range, this material enables the development of all-solid-state sodium-ion batteries with ultra-thick cathodes, delivering reliable functionality at room temperature and in subzero environments. This study expands our understanding of hydroborate-based solid electrolytes, highlighting their potential for high ionic conductivity and broad electrochemical stability windows in next-generation energy storage systems.

Main

All-solid-state batteries (ASBs), with a solid electrolyte replacing the liquid electrolyte in conventional batteries, have attracted considerable attention in academia and industry due to their promising intrinsic characteristics, including enhanced safety, longer lifecycle, and high energy density. While lithium-based batteries remain the dominant technology, sodium-based ASBs are a complementary, safe, and cost-effective alternative chemistry due to the abundance and cost of sodium[10,11]. The general rule in the selection of optimal solid electrolytes depends on several factors: ionic conductivity, electrochemical and chemical stability, and mechanical properties[12,13].

Due to poor sodium diffusivity and high Young's modulus of oxide cathodes, a solid electrolyte must be integrated with the active material to provide ionic percolation in the electrode layer. Thus, solid electrolytes must possess low modulus to conform effectively to the cathode while preserving the intimate contact between the materials during repeated electrochemical reactions. For the ASBs to displace conventional lithium-ion batteries, a thick and dense cathode, along with the use of a high-capacity alloy anode, is necessary to enhance the energy density at the cell level. Accordingly, a highly conductive (>mS cm^{-1}) solid electrolyte is highly sought after to minimize ohmic resistance and polarization in battery cells.

Sodium closo-hydroborates are promising solid electrolytes owing to their low gravimetric density (~1.2 g cm^{-3}), low toxicity, excellent reduction stability, and moderately soft mechanical properties allowing for densification at room temperature[6,14,15]. Superionic conductivity in these materials is generally observed in the close-packed anion or body-centered cubic framework which possesses large Na^+ site vacancies, higher structural symmetry, and the propensity for anion reorientation that promotes Na^+ diffusion[6,8,16-18]. However, the diffusion of the Na^+ in close-packed structures is limited to the high occupancy of the energetically favorable tetrahedral sites in the octahedral-tetrahedral-octahedral diffusion channels, which leads to a high activation energy[4,5,19,20].

Recent research has revealed that non-close-packed frameworks possess a reduced symmetry creating structural distortion leading to irregular coordination between mobile ions and anions thereby yielding higher ionic conductivity[4,5]. However, the orthorhombic sodium closo-hydroborate with $Cmc2_1$ symmetry (o-NBH, with a chemical composition of $Na_3(B_{12}H_{12})(BH_4)$) (**Fig. 1a**) exhibits one order of magnitude lower room temperature ionic conductivity than the close-packed phases[21]. The unclear purity of previously synthesized o-NBH at room temperature raises the possibility of structural instability. In this work, we combine experimental and computational approaches to demonstrate that metastable o-NBH exhibits superionic conductivity, reaching 4.6 mS cm^{-1} at 30 °C. This material facilitates the development of ASBs with an ultra-thick cathode (approximately 310 μm) that deliver reliable capacity not only at room temperature but also in subzero environments.

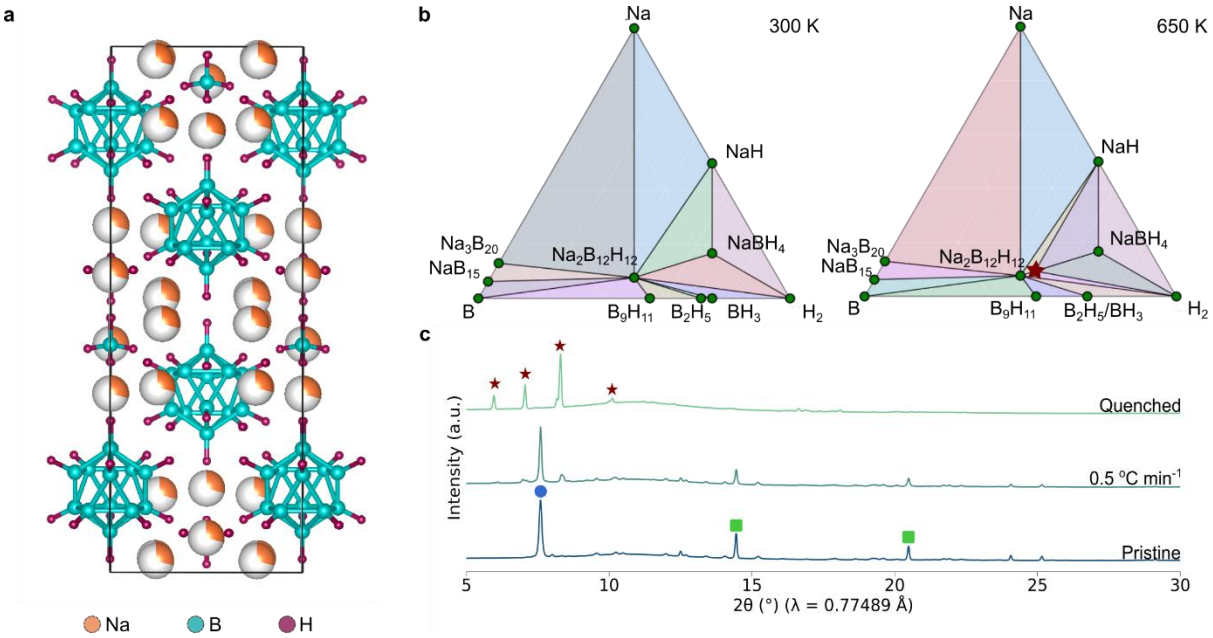

Fig. 1 | Phase stability of o-NBH solid electrolyte. a, Crystal structure of o-NBH with partial sodium occupancy. **b**, Na-B-H compositional phase diagram based on the phonon thermodynamic properties. The calculated stable phases are indicated by the green dot and o-NBH is indicated by ★. **c**, Room temperature XRD pattern of o-NBH with different cooling rates (★ - o-NBH[21], ● - $Na_2B_{12}H_{12}$ (ICSD 164649), and ■ - $NaBH_4$ (ICSD 182734))

Synthesis and Structure Analysis

The phase diagrams of Na-B-H in **Fig. 1b**, derived from highly accurate high-throughput density function theory (DFT) calculations (see *Methods*), suggest that o-NBH is not thermodynamically stable with energy above hull of 16 meV atom^{-1} at 300 K, but is entropically stabilized at temperatures above 650 K. Differential scanning calorimetry (DSC) and synchrotron X-ray diffraction (XRD) patterns were collected to determine the phase evolution with temperature. DSC and in-situ XRD in **Supplementary Figs. 1a and b**, respectively, show that the formation of the o-NBH phase begins at approximately 360 °C and is fully formed at 400 °C. After the formation of o-NBH, rapid cooling of the material by quenching the glass capillary in 25 °C water leads to only the o-NBH phase without any observable precursor reflections (**Fig. 1c** and **Supplementary Fig. 1c**). However, a slow cooling rate (0.5 °C min^{-1}) from 400 °C to room temperature leads to a mixture of $Na_2B_{12}H_{12}$ and $NaBH_4$, implying that o-NBH is a metastable phase that dissociates into its enthalpy-preferred precursors if given sufficient energy and time.

The local environments of the materials prepared with different cooling rates (denoted o-NBH-2 and o-NBH-Q with 2 °C min^{-1} cooling and quenching of o-NBH, respectively) were further probed using ^{11}B, ^{1}H, and ^{23}Na solid-state nuclear magnetic resonance (ss-NMR) spectroscopy. The ^{11}B ss-NMR spectra of $Na_2B_{12}H_{12}$ and $NaBH_4$ in **Fig. 2a** each exhibit a single resonance with chemical shifts of −16.3 ppm and −42.1 ppm (ref. [22,23]), respectively. o-NBH-Q has two resonances centered at −15.5 ppm and −44.3 ppm, which are attributed to boron in $B_{12}H_{12}$ and BH_4 clusters, respectively. The similarity between ^{11}B spectra in the precursors and o-NBH phase suggests that the $B_{12}H_{12}$ and BH_4 clusters are maintained after thermal treatment but with differentiated neighboring sodium distributions. The more negative chemical shift of $^{11}BH_4$ in o-NBH (–44.3 ppm) vs. in $NaBH_4$ (–42.1 ppm) is attributed to electron density donated by the

additional Na^+ from the $Na_2B_{12}H_{12}$ component around the more localized (harder) BH_4 group in the o-NBH structure. Consequently, the $^{11}B_{12}H_{12}$ exhibits a more positive chemical shift from –16.3 to –15.5 ppm. This hypothesis is supported by CASTEP calculations (**Supplementary Table 1**). Strong evidence that the $B_{12}H_{12}$ and BH_4 clusters are mixed into a single phase at the atomic scale comes from two-dimensional ^1H-^1H dipolar-coupling-mediated spin-exchange spectra (**Supplementary Fig. 2**), which shows strong correlations even at millisecond mixing times. Of great utility is that the distinct chemical shifts of $^{11}BH_4$ in o-NBH *vs.* $NaBH_4$ allow us to directly estimate the fraction of the o-NBH phase to be 90 at.% when quenched *vs.* 61 at.% when cooled at 2 °C min^{-1}.

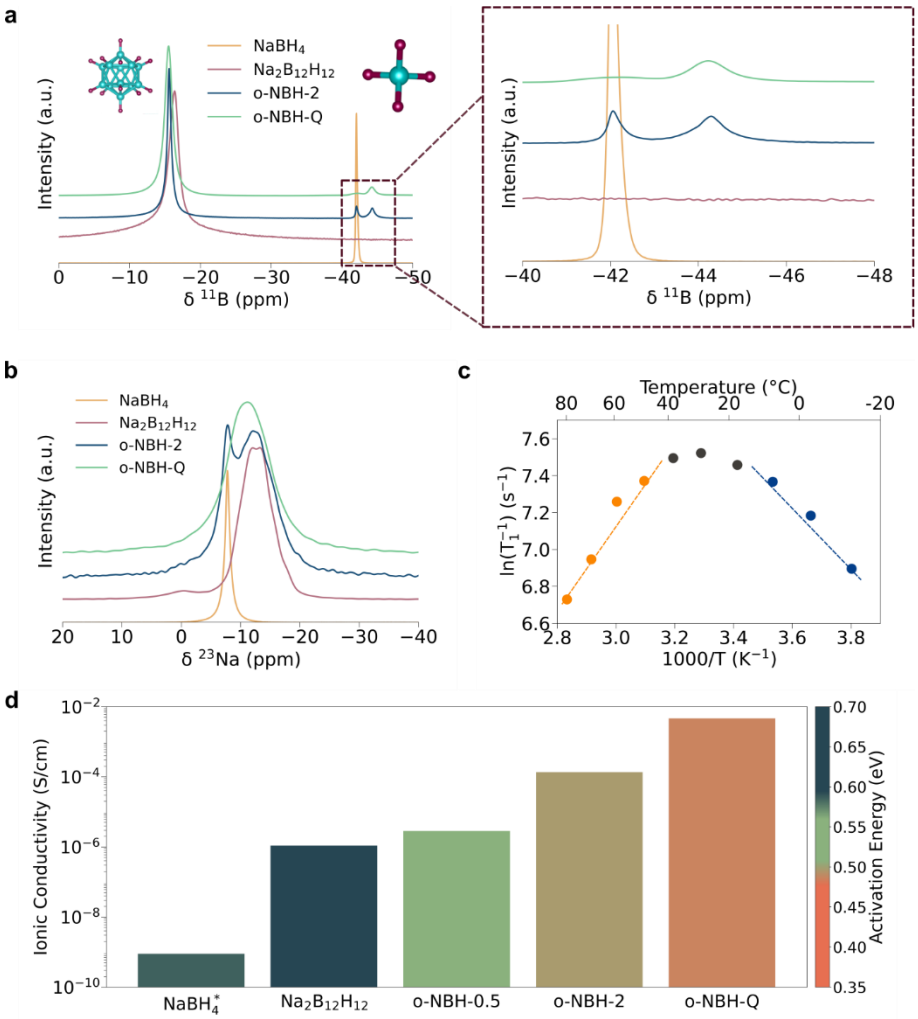

Fig. 2 | Local environment and ionic conductivity of o-NBH prepared with different cooling rates. (**A**) ^{11}B and (**B**) ^{23}Na ss-NMR spectra of the precursors, o-NBH-2, and o-NBH-Q. (**C**) Arrhenius behavior of the ^{23}Na spin-lattice relaxation at variable temperatures. (**D**) Ionic conductivity at 30 °C and activation energy of o-NBH prepared with different cooling rates (0.5, 2 °C min^{-1}, and Ar-gas quenching).

Additionally, ^{23}Na NMR spectra (**Fig. 2b**) indicates the existence of two distinct sodium environments in o-NBH-2, which match $NaBH_4$ and $Na_2B_{12}H_{12}$ at −7.8 ppm and −12.1 ppm, respectively. On the other hand, o-NBH-Q shows a single resonance centered at −11.2 ppm, indicating that there is a chemical exchange and shift averaging between the two environments, which is expected in the proposed structure model featuring neighboring $B_{12}H_{12}$ and BH_4 clusters with rapid Na^+ dynamics. The ^{23}Na line shapes thus support the metastable nature of

the o-NBH phase, which is stabilized at room temperature by rapid cooling. Moreover, ^{23}Na spin-lattice relaxation, which is dominated by fluctuating quadrupolar interactions stimulated by ionic motion in diamagnetic sodium closo-hydroborate, is enhanced by four orders of magnitude in o-NBH-Q (T_1 = 0.56 ms) relative to the precursors (**Supplementary Table 2**). This magnitude of increased relaxation rate is indicative of rapid Na^+ mobility in o-NBH, as seen in other families of sodium superionic conductors[24-26].

Variable temperature spin-lattice relaxation (VT-SLR) of the ^{23}Na was measured to obtain the local activation energy of Na^+ in o-NBH-Q (**Fig. 2c**). Two activation energies can be obtained from VT-SLR; the short-range correlations or localized diffusion are considered for low-temperature where $\omega_o\tau >> 1$ holds, while longer-range correlations are considered for high-temperature where $\omega_o\tau << 1$ holds[27,28]. The short-range and long-range activation energies calculated from VT-SLR are 0.13 and 0.23 eV, respectively, which are lower than the close-packed $Na_4(B_{12}H_{12})(B_{10}H_{10})$ phase, exhibiting hopping barriers of 0.19 and 0.33 eV (ref. [29]), respectively, indicating a lower Na^+ migration barrier in the non-close-packed o-NBH-Q phase reported here. According to the Bloembergen, Purcell, and Pound (BPP) model ($E_a^{LT} = (\beta-1)E_a^{HT}$, β being a measure of the strength of correlation with simple BPP behavior[29-31]), a β value of 1.54 indicates uncorrelated Na^+ motion that stems from Coulomb interactions and/or structural disorder, which will be revisited computationally (*vide infra*). Furthermore, at maximum SLR (T_{max} temperature, 30 °C) where $\tau\omega_o \sim 1$ holds, a jump rate ($1/\tau$) in the order of 10^8 s^{-1} is direct evidence of high ionic conductivity of o-NBH.

To investigate the significance of stabilizing the metastable o-NBH on bulk Na^+ diffusion, the ionic conductivity and activation energy (**Supplementary Fig. 3**) of the o-NBH prepared at different cooling rates were measured. Indeed, the ionic conductivity increases while activation energy decreases with an increasing cooling rate (**Fig. 2d**). The ionic conductivity (at 30 °C) reaches a maximum value of 4.6 mS cm^{-1} when the material was rapidly cooled, which is one of the highest among all sodium solid-state electrolytes reported[32,33]. Direct-current polarization experiments (**Supplementary Fig. 4**) indicate that the electronic conductivity is around 10^{-5} mS cm^{-1}, which is five orders of magnitude lower than the ionic conductivity, indicating it is highly electronically insulating. These results support that the resultant ionic conductivity highly correlates to the purity of the o-NBH, which is a function of the cooling rate used during synthesis.

Ion Diffusion Mechanism

The Na^+ diffusion mechanism in the o-NBH crystal structure was systematically investigated using molecular dynamic (MD) simulations with Materials 3-body Graph Network (M3GNet) graph deep learning interatomic potential (GIP). The o-NBH structure has 1/3 Na^+ occupancy among the seven sites in o-NBH[21], and the high density of accessible sites within the structure provides multiple pathways for Na^+ hopping. Additionally, o-NBH exhibits a large variation in the instantaneous coordination number of $Na{-}B_{12}H_{12}$ and $Na{-}BH_4$ (**Supplementary Fig. 5**) providing a flexible coordination environment and lowering the energy barrier for the fast Na^+ diffusion[16]. Compared to $NaBH_4$ and $Na_2B_{12}H_{12}$, which have no Na^+ site vacancies for ion diffusion (**Supplementary Fig. 6**), the o-NBH structure exhibits a fast macroscopic three-dimensional (3D) Na^+ ion diffusion network, as indicated by the yellow isosurfaces in the Na^+ probability density function (**Fig. 3a**). Beyond the intrinsic Na^+ site vacancies that facilitate Na^+ ion diffusion, dynamic anion motion may disrupt Na^+ site ordering, further flattening the

overall energy landscape[16]. While angular displacement exists in the anion clusters, the tracked hydrogen atom trajectory for 1 ns indicates the motion is highly randomized, which may not have a periodical promotion in the diffusion (**Supplementary Fig. 7**). Combining the high Na^+ site vacancy density, low activation energy, and anion motion, o-NBH exhibits orders of magnitude higher theoretical room temperature ionic conductivity than its monoclinic-$Na_2B_{12}H_{12}$ and cubic-$NaBH_4$ precursors (**Fig. 3b**).

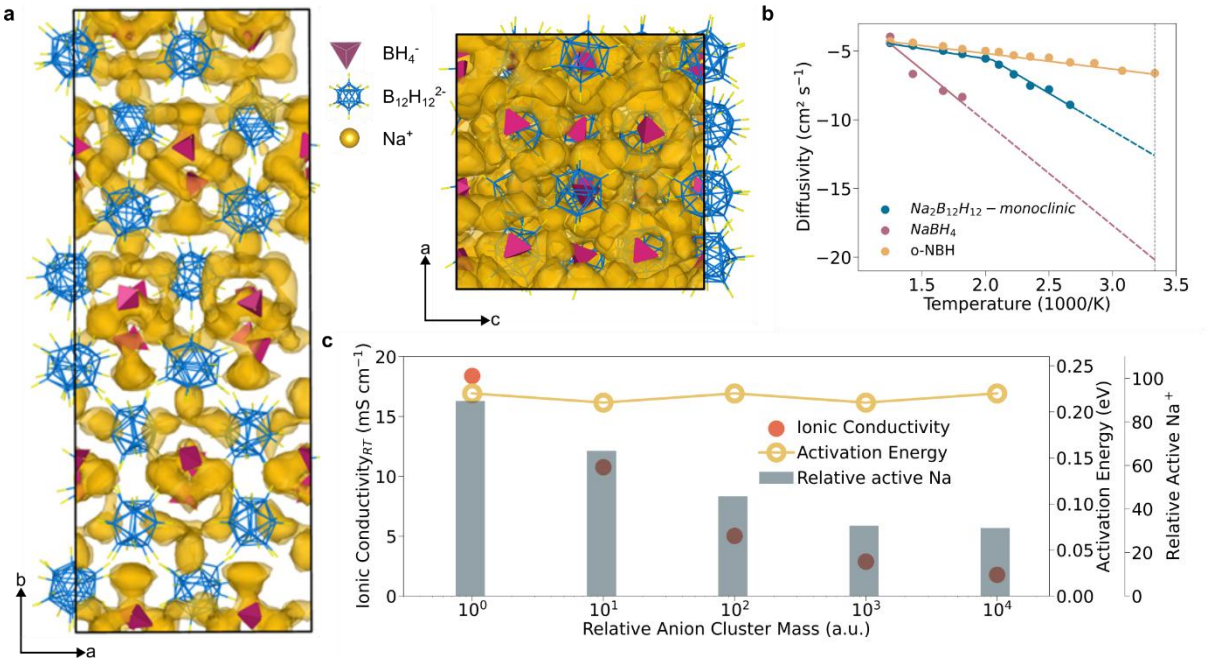

Fig. 3 | o-NBH crystal structure and ionic diffusion mechanism. a, Iso-surface of the Na-probability density function (threshold = 0.5 Å) obtained from 2 ns MD simulation at 300 K. The BH_4 and $B_{12}H_{12}$ anions are shown as fixed red and blue polyhedral, respectively. **b**, Arrhenius plots of diffusivity *vs.* temperature for NBH structures. **c**, Computed room-temperature 300 K ionic conductivity, activation energy, and relative active Na^+ with higher anion cluster mass.

To better understand the influence of the two distinct polyanion polyhedral (BH_4^- and $B_{12}H_{12}^{2-}$) in o-NBH on the Na^+ diffusion dynamics, a series of gedankenexperiment was performed by artificially scaling the mass of each type of polyanion in the MD simulations. Unlike previous works whereby anions were "frozen" in MD[34,35], this approach allows for gradual adjustments to the anion rotational dynamics by modifying their moment of inertia without affecting the chemical interactions between the Na^+ and anions (**Supplementary Fig. 8**). The simulations show that increasing anion mass (and decreasing anion rotation) has a small effect on the activation barrier for diffusion, even though there is a marked decrease in ionic conductivity (**Fig. 3c**). Instead, the reduction in ionic conductivity is highly correlated to the reduction in the number of active Na^+ with increasing anion mass. By independently modifying the BH_4 and $B_{12}H_{12}$ masses, it was found that increasing the mass of the larger $B_{12}H_{12}$ anion has a more pronounced effect on the number of inactive Na and ionic conductivity (**Supplementary Figure 9**).

Electrochemical Characterization

While high ionic conductivity is a crucial intrinsic property for a practical solid electrolyte, the electrochemical stability window impacts the viability of electrodes with high and low sodium chemical potential and, therefore, the accessible battery voltage and energy density. Linear sweep voltammetry indicates that the highly ionic conductive o-NBH exhibits good reduction stability against Na_9Sn_4 but limited oxidation stability, up to 2.5 V *vs.* Na_9Sn_4 (**Fig. 4a**). The reduction stability is further demonstrated with symmetrical Na_9Sn_4/o-NBH/Na_9Sn_4 cell cycling that showed stable and reversible charge transfer after 100 cycles of 1 mAh cm^{-2} of (de)sodiation (**Supplementary Fig. S10a**).

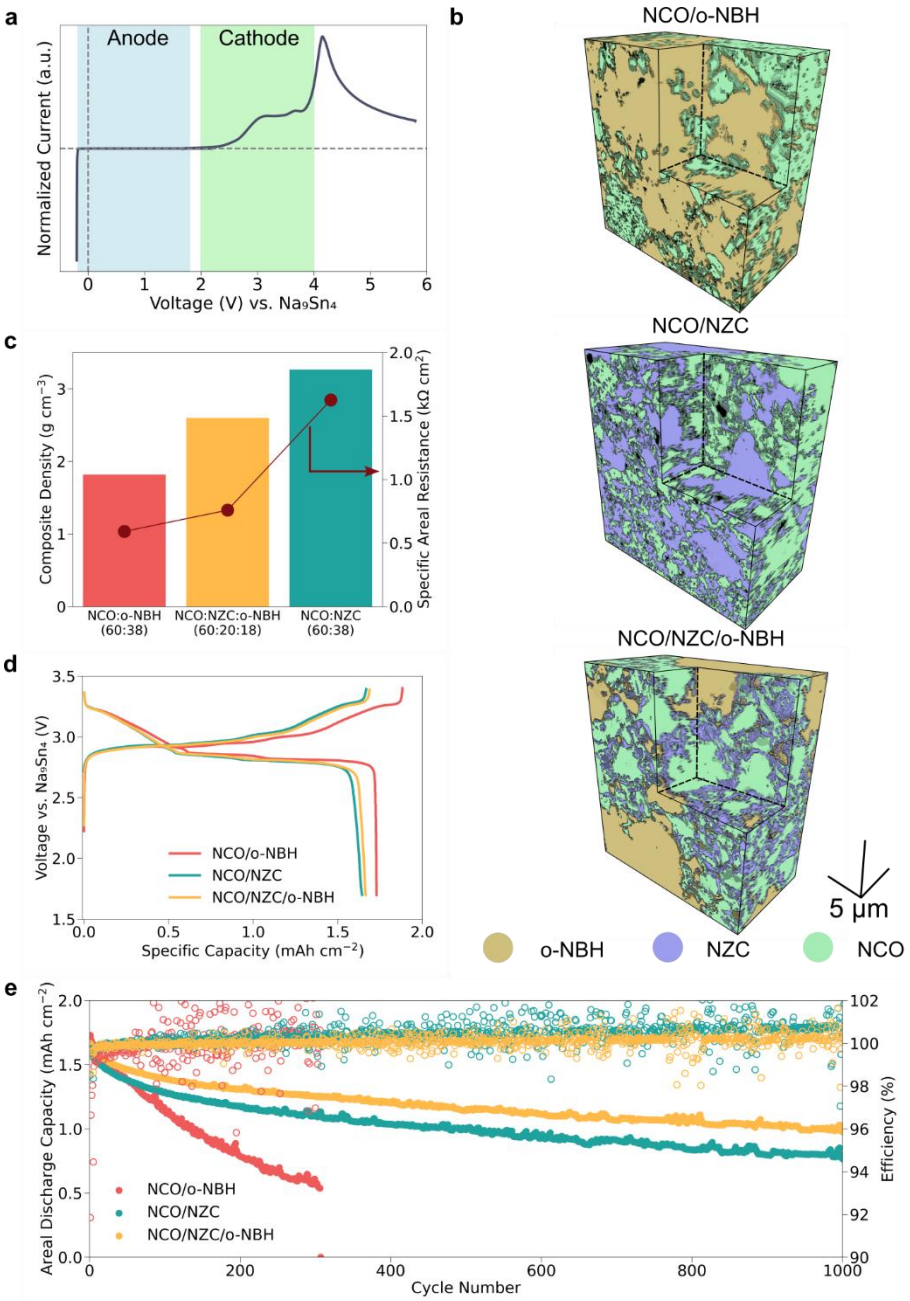

Fig. 4 | Electrochemical stability of o-NBH solid electrolyte and cathode composite FIB-SEM Tomography. a, Linear sweep voltammetry of o-NBH with typical electrode redox potentials highlighted (**Supplementary Table 3**). **b**, 3D reconstructed models of NCO/NBH, NCO/NZC, and NCO/NZC/NBH. **c**, Composite density and specific areal resistance increase

with increasing NZC content due to the differences in the gravimetric density and ionic conductivity. **d**, Initial potential–capacity profiles of Na_9Sn_4/o-NBH/NCO. **e**, Reversible capacity retention of the cathode composites at C/3 in Na-excess cells with Na_9Sn_4 anodes.

According to the grand potential calculation at 300 K (**Supplementary Figure 10b**), the oxidations lower than 3.8 V *vs.* Na^+/Na of o-NBH are hypothesized to form a passivating $Na_2B_{12}H_{12}$. The electrochemical oxidation is further probed by galvanostatic cycling with different maximum cut-off voltages ($V_{cut\text{-}off}$) to study the implications of the various oxidation products. Initial desodiation capacities of 38 and 90 mAh g^{-1} are observed with V_{max} of 3.4 and 4.9 V *vs.* Na_9Sn_4, respectively; negligible capacity is accessible in the subsequent cycle (**Supplementary Fig. 10c**). This is further supported by the slight increase in the interfacial impedance after oxidation at 3.4 V *vs.* Na_9Sn_4 as $Na_2B_{12}H_{12}$ is still slightly ionically conductive (**Supplementary Fig. 10d**); a large interfacial impedance was only observed after oxidizing o-NBH to 4.9 V *vs.* Na_9Sn_4.

The possible passivating oxidation products of o-NBH are further investigated by assembling an all-solid-state battery using bare $NaCrO_2$ (NCO) and oxidation-resistant Na-Zr-Cl solid-electrolyte-coated NCO (NCO/NZC) as the cathode. The distribution of the materials and the intimate contact between them in the composite were visualized by reconstructing the cross-sectional scanning electron microscopy images prepared by focused ion beam milling (**Fig. 4b**). While the gravimetric ratio of the NCO, solid electrolyte, and carbon in the composite is constant, there is more solid electrolyte volumetric content when o-NBH is added in the cathode composite stemming from the different gravimetric density of components (NZC – ~2.4 g cm^{-3} and o-NBH – ~1.2 g cm^{-3}). Consequently, NCO/o-NBH, NCO/NZC, and NCO/NZC/o-NBH have higher ionic tortuosity values of 1.53, 4.91, and 3.46, respectively. This is also reflected in the cathode composite volumetric density and impedance with NCO/o-NBH having the lowest density and areal resistivity in the series followed by NCO/NZC/o-NBH and then NCO/NZC (**Fig. 4c**). This trend is attributed to the higher ionic conductivity and high volumetric content of o-NBH compared to NZC facilitating fast ion diffusion in the cathode composite.

Sodium-Excess Cell (Half Cell)

To evaluate the oxidation stability of o-NBH, half-cell ASBs with a cathode mass loading of 15 mg_{NCO} cm^{-2} (theoretical capacity of 2.3 mAh cm^{-2}) were assembled using NCO/o-NBH, NCO/NZC, or NCO/NZC/o-NBH as the cathode and Na_9Sn_4 as the counter electrode. Fig. 4D shows that all the cells have good material utilization (92.5 to 104.2% of the theoretical NCO capacity) with the NCO/o-NBH cell exhibiting a slightly higher charge capacity than that of NCO/NZC and NCO/NZC/NBH. In the subsequent reverse cycle, the NCO/o-NBH exhibits the lowest initial coulombic efficiency (ICE) of 91.9% while NCO/NZC and NCO/NZC/o-NBH have higher ICEs of ~98.2%. This implies the higher-than-theoretical charge capacity in NCO/o-NBH stems from the oxidation of o-NBH. The impact of ionic tortuosity and interfacial compatibility is highlighted in the subsequent C/3 cycling. The interfacial incompatibility between NCO and o-NBH leads to rapid capacity fading as reflected by the NCO/o-NBH cell, retaining less than 1 mAh cm^{-2} (~60% of initial capacity) after 140 cycles with an average coulombic efficiency of 99.6% (Fig. 4E). Credited to the stable electrochemical interface, both NCO/NZC and NCO/NZC/o-NBH cells exhibited more stable cycling retaining 1.23 and 1.36 mAh cm^{-2} after 140 cycles, respectively, and 0.82 and 1.20 mAh cm^{-2} after 1000 cycles,

respectively. While the first cycle differential capacity dQ/dV plot showed similar redox reactions in each cathode–solid-electrolyte composite (**Supplementary Fig. S11a**), the NCO/o-NBH suffered from larger dQ/dV profiles polarization than that of the others (**Supplementary Fig. S11b-d**). Furthermore, the NCO/o-NBH cell shows a faster rate of constant-voltage capacity and an increase in cell impedance with cycle number (**Supplementary Figs. S11e and f**), likely fueled by the continuous formation of non-passivating and ionically insulating interphases due to o-NBH oxidation.

Thick-Cathode Zero-Excess-Sodium Cell (Full Cell)

For ASBs to displace conventional Li-ion batteries, they must realize a high areal capacity using a thick cathode, minimizing inactive components at the cell level (**Fig. 5a** and **Supplementary Fig. S12**), and possess the ability to operate in extreme environments. Thus, we leverage the balance of ionic conductivity and electrochemically stable interface of the NCO/NZC/o-NBH cathode composite to assemble sodium-inventory-limited ASBs with high cathode areal capacity loading (15, 30, and 45 mg_{NCO} cm^{-2}, corresponding to thicknesses of approximately 123±0.8, 217±2.6 and 310±2.0 µm, respectively, **Fig. 5b**) and tin as the anode. While material utilization is slightly affected by the increased cathode thickness due to polarization, all cells exhibit a similar ICE (70–81%) owed to sluggish Na^+ diffusion kinetics of the Sn anode at low states-of-charge (SOC), limiting the Na^+ diffusion at the 2D electrode/electrolyte interface (**Fig. 5c**, **Supplementary Figs. S13 and S14a-c**). Nevertheless, the ASBs still deliver high reversible capacities of 1.3, 2.2, and 3.5 mAh cm^{-2} at 15, 30, and 45 mg_{NCO} cm^{-2} loadings, respectively. These are amongst the highest reported sodium ASB active material areal loadings (**Supplementary Fig. S14d**) and feature reversible capacities that are close to or higher than conventional Li-ion batteries. Following the initial cycle, all cells have an average coulombic efficiency of 99.8–99.9% resulting in a capacity retention of >80% after 100 cycles (**Fig. 5d**).

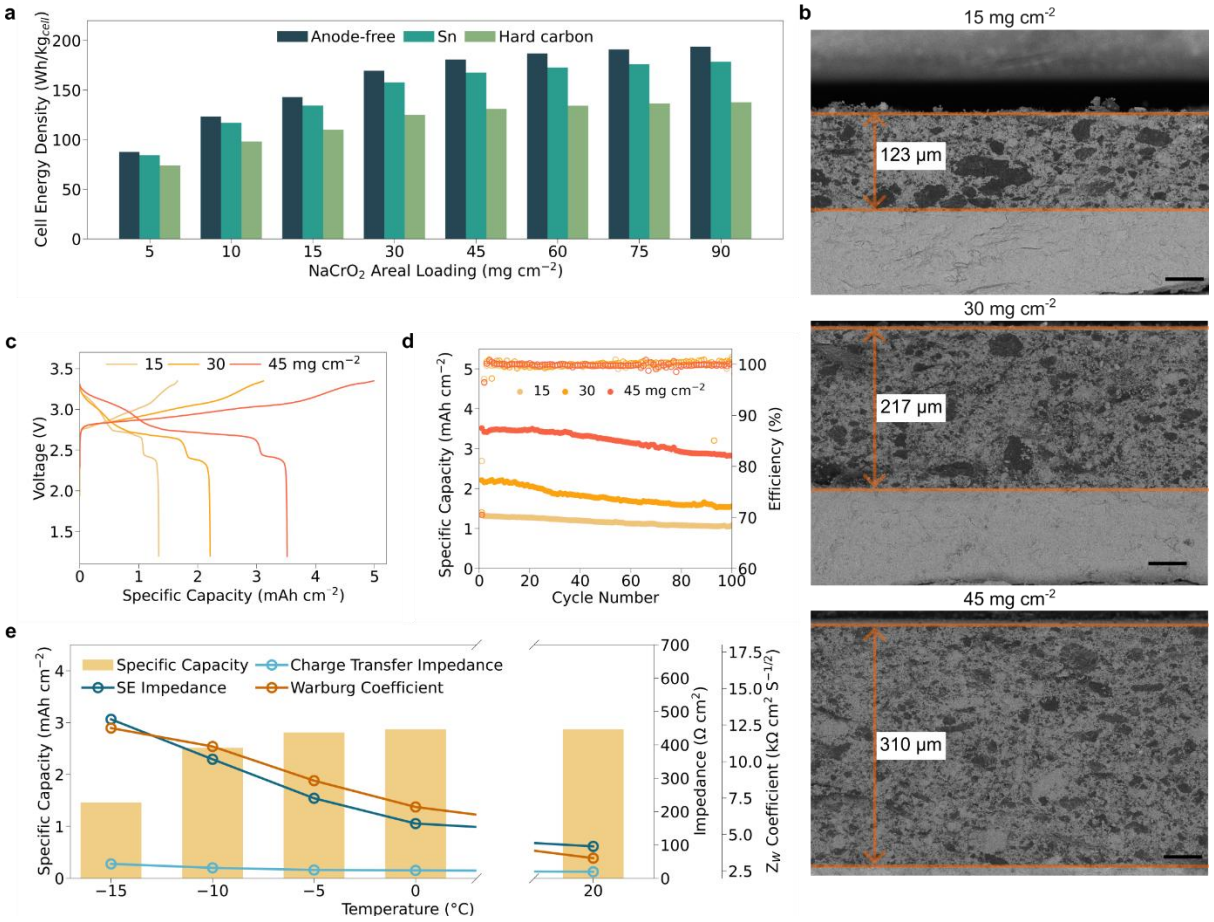

Fig. 5 | Electrochemical stability of high-loading Na ASB full-cell. a, Cell capacity increases with increasing $NaCrO_2$ areal loading (using 60 wt.% $NaCrO_2$ cathode composite). **b,** Cathode thickness with various areal loadings, scale bar = 50 µm. **c,** Initial potential–capacity profiles and the capacity retention with various loadings. **d,** Capacity retention of the full cells at C/10. **e,** Discharge capacity and cell impedance of a full cell with 45 mg_{NCO} cm^{-2} at sub-ambient temperatures.

The capability of the high areal capacity cell configuration (45 mg_{NCO} cm^{-2}) is further demonstrated at sub-zero temperatures, highlighting its viability in cold climates. The cell (**Fig. 5e**) delivers high discharge capacities of 3.1, 2.9, 2.8, 2.5, and 1.5 mAh cm^{-2} at room temperature, 0, −5, −10, and −15 °C, respectively. The decrease in capacity at lower temperatures is attributed to increased cell impedance (**Supplementary Fig. 15**). Further examination of the EIS spectra also reveals that the Warburg diffusion coefficient in the electrodes also increases significantly at −15 °C compared to room temperature. This suggests that the bulk diffusion in the electrode is one of the capacity-limiting factors when operating at low temperatures. Alternative electrode active materials with fast bulk diffusion at all states-of-charge or novel electrode architectures should be considered to further improve the kinetics. Nevertheless, this work highlights that high-loading all-solid-state batteries can operate in cold climates without external heating or severe discharge capacity penalty.

Conclusion

In conclusion, we successfully stabilized a metastable orthorhombic hydroborate structure, o-NBH, through precise control of synthesis conditions. The non-close-packed anion framework exhibits exceptional ionic conductivity across a wide temperature range, from 0.3 mS cm^{-1} at

−10 °C to 4.6 mS cm^{-1} at 30 °C. Notably, the propensity of anion's motion enhances the population of highly mobile Na^+, thereby increasing the ionic conductivity, without lowering the Na^+ activation energy. Incorporating o-NBH into the NCO/NZC cathode composite effectively balances the electrochemical stability with sodium ion kinetics in the thick cathode composite. An all-solid-state sodium-ion full-cell battery with a high NCO loading (45 mg_{NCO} cm^{-2}, ~310 µm thick) and Sn as cathode and anode, respectively, delivers a discharge capacity of 3.1 and 2.5 mAh cm^{-2} at room temperature and −10 °C, respectively. This study broadens the scope of the solid electrolyte design, extending beyond hydroborate-based chemistry, and introduces new approaches to cell architecture that have the potential to drive the next generation of batteries.

References

1 Deysher, G. *et al.* Design principles for enabling an anode-free sodium all-solid-state battery. *Nature Energy*, doi:10.1038/s41560-024-01569-9 (2024).

2 Tan, D. H. S., Meng, Y. S. & Jang, J. Scaling up high-energy-density sulfidic solid-state batteries: A lab-to-pilot perspective. *Joule* **6**, 1755-1769, doi:10.1016/j.joule.2022.07.002 (2022).

3 Li, Y. *et al.* A lithium superionic conductor for millimeter-thick battery electrode. *Science* **381**, 50-53, doi:10.1126/science.add7138 (2023).

4 Luo, J. D. *et al.* Halide Superionic Conductors with Non-Close-Packed Anion Frameworks. *Angewandte Chemie International Edition* **63**, doi:10.1002/anie.202400424 (2024).

5 Wang, Y. *et al.* Design principles for solid-state lithium superionic conductors. *Nat Mater* **14**, 1026-1031, doi:10.1038/nmat4369 (2015).

6 Brighi, M., Murgia, F. & Černý, R. Closo-Hydroborate Sodium Salts as an Emerging Class of Room-Temperature Solid Electrolytes. *Cell Reports Physical Science* **1**, doi:10.1016/j.xcrp.2020.100217 (2020).

7 Yoshida, K. *et al.* Fast sodium ionic conduction in $Na_2B_{10}H_{10}$-$Na_2B_{12}H_{12}$ pseudo-binary complex hydride and application to a bulk-type all-solid-state battery. *Applied Physics Letters* **110**, doi:10.1063/1.4977885 (2017).

8 Duchene, L. *et al.* A highly stable sodium solid-state electrolyte based on a dodeca/deca-borate equimolar mixture. *Chem Commun (Camb)* **53**, 4195-4198, doi:10.1039/c7cc00794a (2017).

9 Asakura, R. *et al.* 4 V room-temperature all-solid-state sodium battery enabled by a passivating cathode/hydroborate solid electrolyte interface. *Energy & Environmental Science* **13**, 5048-5058, doi:10.1039/d0ee01569e (2020).

10 Jakob, F. *et al.* Battery 2030: Resilient, sustainable, and circular. 2-18 (McKinsey & Company, 2023).

11 Hirsh, H. S. *et al.* Sodium-Ion Batteries Paving the Way for Grid Energy Storage. *Advanced Energy Materials* **10**, doi:10.1002/aenm.202001274 (2020).

12 Oh, J. A. S., He, L., Chua, B., Zeng, K. & Lu, L. Inorganic sodium solid-state electrolyte and interface with sodium metal for room-temperature metal solid-state batteries. *Energy Storage Materials* **34**, 28-44, doi:10.1016/j.ensm.2020.08.037 (2021).

13 Janek, J. & Zeier, W. G. Challenges in speeding up solid-state battery development. *Nature Energy* **8**, 230-240, doi:10.1038/s41560-023-01208-9 (2023).

14 Deysher, G. *et al.* Evaluating Electrolyte-Anode Interface Stability in Sodium All-Solid-State Batteries. *ACS Appl Mater Interfaces* **14**, 47706-47715, doi:10.1021/acsami.2c12759 (2022).

15 Oh, J. A. S. *et al.* High-Performing All-Solid-State Sodium-Ion Batteries Enabled by the Presodiation of Hard Carbon. *Advanced Energy Materials* **13**, doi:10.1002/aenm.202300776 (2023).

16 Kweon, K. E. *et al.* Structural, Chemical, and Dynamical Frustration: Origins of Superionic Conductivity in closo-Borate Solid Electrolytes. *Chemistry of Materials* **29**, 9142-9153, doi:10.1021/acs.chemmater.7b02902 (2017).

17 Campos dos Santos, E. *et al.* Explore the Ionic Conductivity Trends on $B_{12}H_{12}$ Divalent Closo-Type Complex Hydride Electrolytes. *Chemistry of Materials* **35**, 5996-6004, doi:10.1021/acs.chemmater.3c00975 (2023).

18 Udovic, T. J. *et al.* Sodium superionic conduction in $Na_2B_{12}H_{12}$. *Chem Commun (Camb)* **50**, 3750-3752, doi:10.1039/c3cc49805k (2014).

19 Lu, Z. & Ciucci, F. Structural origin of the superionic Na conduction in $Na_2B_{10}H_{10}$ closo-borates and enhanced conductivity by Na deficiency for high performance solid electrolytes. *Journal of Materials Chemistry A* **4**, 17740-17748, doi:10.1039/c6ta07443j (2016).

20 Wang, S. *et al.* Design principles for sodium superionic conductors. *Nat Commun* **14**, 7615, doi:10.1038/s41467-023-43436-3 (2023).

21 Sadikin, Y., Brighi, M., Schouwink, P. & Černý, R. Superionic Conduction of Sodium and Lithium in Anion-Mixed Hydroborates $Na_3BH_4B_{12}H_{12}$ and $(Li_{0.7}Na_{0.3})_3BH_4B_{12}H_{12}$. *Advanced Energy Materials* **5**, doi:10.1002/aenm.201501016 (2015).

22 Łodziana, Z., Błoński, P., Yan, Y., Rentsch, D. & Remhof, A. NMR Chemical Shifts of 11B in Metal Borohydrides from First-Principle Calculations. *The Journal of Physical Chemistry C* **118**, 6594-6603, doi:10.1021/jp4120833 (2014).

23 Jensen, S. R. H. *et al.* Hydrogenation properties of lithium and sodium hydride - closo-borate, $[B_{10}H_{10}]^{2-}$ and $[B_{12}H_{12}]^{2-}$, composites. *Phys Chem Chem Phys* **20**, 16266-16275, doi:10.1039/c7cp07776a (2018).

24 Yu, C., Ganapathy, S., de Klerk, N. J. J., van Eck, E. R. H. & Wagemaker, M. Na-ion dynamics in tetragonal and cubic Na_3PS_4, a Na-ion conductor for solid state Na-ion batteries. *Journal of Materials Chemistry A* **4**, 15095-15105, doi:10.1039/c6ta05896e (2016).

25 Zhou, L., Bazak, J. D., Li, C. & Nazar, L. F. 4 V Na Solid State Batteries Enabled by a Scalable Sodium Metal Oxyhalide Solid Electrolyte. *ACS Energy Letters* **9**, 4093-4101, doi:10.1021/acsenergylett.4c01855 (2024).

26 Ridley, P. *et al.* Tailoring Chloride Solid Electrolytes for Reversible Redox. doi:10.26434/chemrxiv-2024-v3s5m (2024).

27 Kuhn, A. *et al.* Li self-diffusion in garnet-type $Li_7La_3Zr_2O_{12}$ as probed directly by diffusion-induced Li^7 spin-lattice relaxation NMR spectroscopy. *Physical Review B* **83**, doi:10.1103/PhysRevB.83.094302 (2011).

28 Ganapathy, S., Yu, C., van Eck, E. R. H. & Wagemaker, M. Peeking across Grain Boundaries in a Solid-State Ionic Conductor. *ACS Energy Letters* **4**, 1092-1097, doi:10.1021/acsenergylett.9b00610 (2019).

29 Duchêne, L. *et al.* Ionic Conduction Mechanism in the $Na_2(B_{12}H_{12})_{0.5}(B_{10}H_{10})_{0.5}$ closo-Borate Solid-State Electrolyte: Interplay of Disorder and Ion–Ion Interactions. *Chemistry of Materials* **31**, 3449-3460, doi:10.1021/acs.chemmater.9b00610 (2019).

30 Zhang, S. *et al.* A family of oxychloride amorphous solid electrolytes for long-cycling all-solid-state lithium batteries. *Nat Commun* **14**, 3780, doi:10.1038/s41467-023-39197-8 (2023).

31 Bloembergen, N., Purcell, E. M. & Pound, R. V. Relaxation Effects in Nuclear Magnetic Resonance Absorption. *Physical Review* **73**, 679-712, doi:10.1103/PhysRev.73.679 (1948).

32 Liu, G., Yang, J., Wu, J., Peng, Z. & Yao, X. Inorganic Sodium Solid Electrolytes: Structure Design, Interface Engineering and Application. *Adv Mater* **36**, e2311475, doi:10.1002/adma.202311475 (2024).

33 Huang, J. *et al.* Recent progress and strategic perspectives of inorganic solid electrolytes: fundamentals, modifications, and applications in sodium metal batteries. *Chem Soc Rev* **52**, 4933-4995, doi:10.1039/D2CS01029A (2023).

34 Smith, J. G. & Siegel, D. J. Low-temperature paddlewheel effect in glassy solid electrolytes. *Nature Communications* **11**, doi:10.1038/s41467-020-15245-5 (2020).

35 Zhang, Z., Roy, P. N., Li, H., Avdeev, M. & Nazar, L. F. Coupled Cation-Anion Dynamics Enhances Cation Mobility in Room-Temperature Superionic Solid-State Electrolytes. *J Am Chem Soc* **141**, 19360-19372, doi:10.1021/jacs.9b09343 (2019).

Methods

Material synthesis. All fabrication processes were conducted in an Ar-filled glovebox (H_2O and O_2 <5 ppm). To make the $Na_3(B_{12}H_{12})(BH_4)$, stoichiometric amounts of $Na_2B_{12}H_{12}$ (Boron Specialties LLC, dried at 175 °C under dynamic vacuum for two nights) and $NaBH_4$ (99.99%, Sigma Aldrich) were hand-mixed using a pestle and mortar. Then, the mixture was sealed in an evacuated quartz ampoule before the thermal treatment. The material was heated to 410 °C at 3 °C min^{-1} and held for 10 h before cooling at 0.5 and 2.0 °C min^{-1}. To achieve rapid cooling, the material was quenched in the Ar-filled glovebox after the thermal treatment.

Na_9Sn_4 anode was prepared by ball milling sodium metal and tin (Sn, Sigma Aldrich) using Retsch EMAX ball milling at 500 rpm for 3 h with a 30:1 Ø5 mm 20:1 (ball:material) ratio. $NaCrO_2$ (NCO) was prepared by solid-state reaction of a pestle and mortar mixed with Na_2CO_3 and Cr_2O_3 at 900 °C in an argon environment for 10 h. Na-Zr-Cl solid electrolyte (NZC) was prepared by ball milling stoichiometric amounts of NaCl and $ZrCl_4$ using an Retsch EMAX ball miller at 550 rpm for 20 h with a 30:1 Ø5 mm ball:material weight ratio.

Materials Characterization

Crystal structure analysis. The high-resolution synchrotron powder X-ray diffraction (s-XRD) and in-situ heating powder X-ray diffraction were performed at beamline TPS-19A in Taiwan Photon Source (TPS), National Synchrotron Radiation Research Center (NSRRC). The energy for all PXRD was calibrated to 16 keV (0.77489 Å), with the geometry and sample position offset corrections calibrated using NIST standard material, LaB_6 (660c). A hot air gas blower was placed 2 mm under the capillary sample with a uniform ramp rate of 5 °C per minute for the in-situ heating experiment. Powder X-ray diffraction patterns were collected every 20 °C along the temperature ramping process. One-dimensional powder X-ray diffraction patterns were recorded by a MYTHEN 18K detector with an exposure time of 60 seconds.

Solid-state nuclear magnetic resonance (NMR) spectra were recorded under magic angle spinning (MAS) in a static magnetic field of 9.4 T with a Bruker Ascend^{TM} 400 MHz magnet and a Bruker Avance NEO NMR spectrometer. The samples were packed into 1.6 mm-diameter zirconia rotors in an Ar-filled environment with polyimide and polyamide-imide caps, and spectra were measured with a Phoenix narrow-bore 1.6 mm HX probe. T_1 (spin-lattice) relaxation was measured with a saturation–recovery pulse sequence for $T_1 > 1$ s or an inversion–recovery pulse sequence for $T_1 < 1$ s. Line broadening of ^{11}B from heteronuclear dipolar coupling and J-coupling was mitigated by proton decoupling (**Extended Data Fig. 1**). All spectra were measured with a direct pulse–acquire pulse sequence using the following rf pulses: ^{23}Na (45°, 0.9 μs, 135 kHz); ^{11}B (90°, 1.73 μs, 145 kHz) with or without ^{1}H decoupling (SPINAL64, 154 kHz). ^{1}H–^{1}H 2D dipolar-coupling-mediated spin-exchange spectra (proton spin diffusion) (90°, 1.36 μs, 184 kHz) with 8 scans per row and 176 rows in the indirect dimension spaced at 50 μs intervals acquired with the States-TPPI mode. Recycle delays were $\geq 5T_1$.

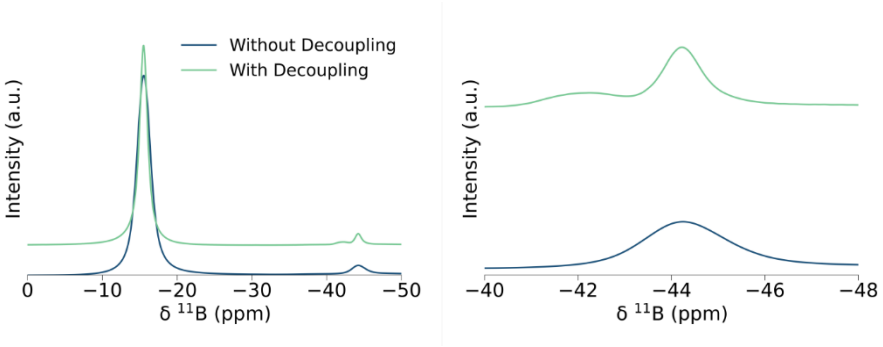

Extended Data Fig. 1 | ^{11}B of NBH-Q with and without ^{1}H decoupling. The B-H heteronuclear dipolar coupling and J-coupling can cause line broadening in the ^{11}B ss-NMR spectra. By applying ^{1}H decoupling, the ^{11}B resonances in various boron environments can be better resolved, resulting in more accurate and precise.

Microstructure analysis. Due to the moisture sensitivity, the sample was transferred from the glovebox to the scanning electron microscopy (SEM) using the QuickLoader. The cross-section is prepared by focus Ga-ion beam milling and SEM images were obtained using an FEI Scios DualBeam Focused ion beam, equipped with an Everhart–Thornley Detector. The different Z-values of the NCO, NZC, and o-NBH allow a different contrast in the backscattered electron beam microscopy. The 3D reconstructed model of the composite is prepared by milling 200 nm per slice for 10 µm. Reconstruction is done using Thermo Scientific™ Avizo software. Ionic tortuosity along the z-direction (separator to current collector) is calculated using the 3D reconstructed model and Tau factor in Matlab[36]. The processing and imaging of the sodiated Sn was conducted at cryogenic temperature.

Electrochemical characterization. Owing to the low modulus nature of o-NBH, the powder was pelletized at 275 MPa at room temperature (**Extended Data Fig. 2**) before electrochemical measurement. The electrochemical impedance spectra (EIS), linear sweep voltammetry (LSV), and DC polarization were conducted using a Biologic VSP200. To measure EIS (from 7 MHz to 1 Hz), around 90 mg of the materials were pelletized under a uniaxial pressure of 275 MPa. Then, acetylene black was added on both ends acting as ion-blocking electrode before compacting at 120 MPa. The thickness of the pellet is estimated by measuring the set-up before adding the powder and after the 275 MPa palletization using a Vernier caliper. The EIS spectra at various temperatures were recorded by keeping the material under the stated temperatures (−10 to 50 °C, at 10 °C per step) for 1 h in an ESPEC temperature chamber.

The reduction and reduction LSV sweep were conducted using o-NBH and stainless-steel powder (SS, Sigma-Aldrich) composite with a weight ratio of 1:1 and o-NBH and acetylene black (AB) composite with a weight ratio of 7:3, respectively. Both composite electrodes were mixed using pestle and mortar and an o-NBH areal loading of 8.9 mg cm^{-2} with Na_9Sn_4 as the counter electrode.

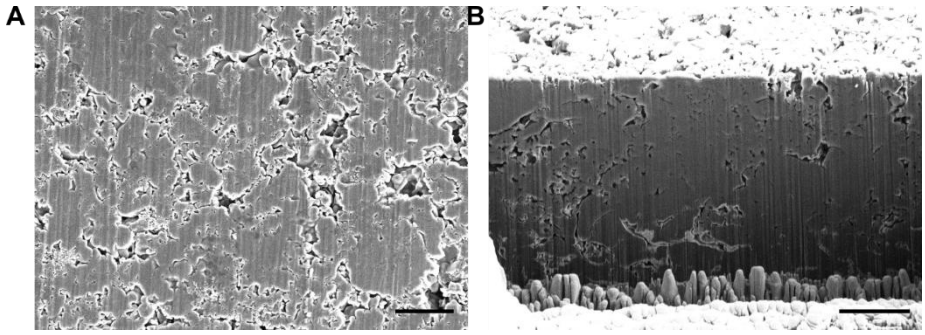

Extended Data Fig. 2 | o-NBH morphology after pressing at 275 MPa at room temperature. Scanning electron microscopy image of o-NBH **a**, surface and **b**, cross-section prepared by focused ion beam milling (scale bar – 10 μm).

Electrochemical characterization

Anode preparation. The Sn anode was prepared by casting Sn with PVdF with a weight ratio of 99:1. The sodium-limited ASSB has a negative:positive electrode capacity (NP) ratio of 1.2 − 1.5, with NCO and Sn having capacities of 120 and 845 mAh g^{-1}, respectively.

Cathode preparation. NCO was chosen due to its relatively low redox potential of 3.2 V *vs.* Na_9Sn_4 which is very close to the first oxidation of o-NBH which is hypothesized to form the $Na_2B_{12}H_{12}$ and B_2H_5 interphases. The NCO:solid electrolyte:vapor-grown carbon fiber (VGCF) cathode composite has a mass ratio 60:38:2. The intimate contact between NCO and NZC was prepared by ball milling NCO and NZC using the PM200 at 160 rpm for 1 h (10 minutes of milling and 2 minutes of rest) with a 20:1 Ø1 mm yttrium-stabilized zirconia ball:material weight ratio. The NCO/NZC/o-NBH cathode composite has the (NCO/NZC):o-NBH:VGCF weight ratio of (60:20):18:2. All composites were hand-mixed using a pestle and mortar.

All-solid-state batteries fabrication. 55-60 mg of o-NBH powder was first pressed into a pellet at 275 MPa in a Ø10 mm peek sleeve using two titanium rods. Then, 19.6, 39.3, and 58.9 mg of the cathode composite to make 15, 30, and 45 mg_{NCO} cm^{-2} for a Ø10 mm cavity, respectively. Anode (35 mg of Na_9Sn_4 or appropriate amount of Sn) was introduced on the other end. The cell was then pressed to 275 MPa.

Cycling protocol. The cells were clamped between two stainless steel plates held by bolts and nuts. For room-temperature cycling, the cells were cycled within the Ar-filled glovebox. The cell is charged with constant current – constant voltage (CCCV) protocol, with the constant voltage set at 3.4 V and cut-off at 0.1 C (where 1 C = 120 mA g^{-1}). The cell was contained within a homemade leakproof enclosure in the Ar-filled glovebox for low-temperature discharge performance before transferring it out. The cell was charged at room temperature and discharged at 0, −5, −10, and −15 °C in an ESPEC temperature chamber. All cells were cycled using a Landt battery cycler under an operating pressure of 75 MPa.

Effective capacity of all-solid-state batteries. To visualize the importance of realizing high-cathode loading cathode in battery, we calculated the estimated cell capacity considering the number of aluminum foil and solid electrolyte separators needed to achieve the target capacity. Three anodes, anode-free, Sn, and hard carbon, with a negative:positive (NP) capacity ratio of 1.1 are considered in this illustration. Based on the previous study[15], hard carbon would work well when mixed with solid electrolyte at a weight ratio of 7:3 so the mass of the hard carbon

anode is corrected accordingly. The energy density of the full cell calculation in **Fig. 5a** is based on the following assumptions:

Aluminum current collector:	2.7 g cm^{-3}, 20 µm
Solid electrolyte separator:	1.3 g cm^{-3}, 50 µm
Negative:positive electrode ratio:	1.1
Tin capacity:	847 mAh g^{-1}
Hard carbon capacity:	250 mAh g^{-1}
Target areal capacity:	7.2 mAh cm^{-2}

Computational methods

Density functional theory calculations of the solid-state NMR. The ss-NMR tensor calculations were carried out in the plane-wave pseudopotential code CASTEP v23.1 (ref. [37]) on DFT-optimized structures taken from the literature[21]. The calculations used the Perdew–Burke–Ernzerhof exchange-correlation functional[38] and ultrasoft on-the-fly pseudopotentials generated in CASTEP with a plane-wave energy cut-off of 800 eV and a Monkhorst–Pack *k*-point grid spacing finer than 0.04 × 2π $Å^{-1}$ (ref. [39]). Geometry optimization was performed with the Limited-memory Broyden–Fletcher–Goldfarb–Shanno (LBFGS) algorithm[40] until the forces on atoms and stresses on the cell converged to better than 0.01 eV $Å^{-1}$ and 100 MPa, respectively. Subsequently, the NMR chemical shielding and quadrupolar interaction tensors were calculated using the gauge-including projector augmented-wave (GIPAW) approach[41-43].

Training structure generation and M3GNet training. The Materials 3-body Graph Network (M3GNet) architecture has already been extensive covered in previous work[44]. To develop a robust training data for Na-B-H M3GNet graph deep learning interatomic potential (GIP), the following data generation protocol was used:

1. First, we extract all crystals in the Na-B-H chemical systems in Materials Project and Inorganic Crystal Structure Database (ICSD)[45,46]. All structures were optimized with revised regularized strongly constrained and appropriately normed (r^2SCAN) functional[44]. The ground state structures, and relaxation trajectories (89 structures) were also included in the training dataset.

2. To expand the configuration space to cover more diverse local environments, particularly at higher temperatures, canonical ensemble (NVT) MD simulations were carried out using the pre-trained M3GNet universal potential[44] on the relaxed structures for 10 ps with a time interval of 10 fs. Simulations were also performed at 5 strains (0, ±0.05, ±0.1) and 5 temperatures (300 K to 900 K with an interval of 150 K). We then sampled the snapshots using the DImensionality-Reduced Encoded Clusters with sTratified (DIRECT) sampling approach described in ref [47] to ensure good coverage of the configuration space.

3. Static self-consistent calculations with r^2SCAN functional were performed on the training structures obtained from Step 2 to obtain the energies, forces, and stresses for M3GNet training. All calculations were performed with an energy cutoff of 680 eV, a *k* spacing of 0.35 $Å^{-1}$, and an electronic relaxation convergence condition of 1×10^{-5} eV $atom^{-1}$ (ref. [48]).

4. The dataset was split into 9:1 as training and testing dataset. The radius cutoff is 5 Å and the three-body cutoff is 4 Å.

The mean absolute error (MAE) of training energies, forces, and stresses were 20.96 meV atom^{-1}, 0.15 eV Å^{-1}, and 1.54 meV Å^{-3}, respectively, while the MAE of the testing set was 30.20 meV atom^{-1}, 0.16 eV Å^{-1}, and 1.80 meV Å^{-3}, respectively.

All training, sampling, evaluations, and simulations with M3GNet were performed using LAMMPS [49], Materials Graph Library (MatGL), and the Materials Machine Learning (maml) Python package.

Density function theory (DFT) calculation. All DFT calculations were performed by Vienna ab initio simulation package (VASP)[50] with projector augmented wave (PAW) potentials. The r^{2}SCAN meta-generalized gradient approximation (GGA)[38] functional was utilized for structural relaxation. Spin-polarized calculations with an energy cutoff of 680 eV, a *k* spacing of 0.35 Å^{-1}, and an electronic relaxation convergence condition of 1×10^{-5} eV atom^{-1} were applied to the structural relaxations.

Na-B-H phase diagram calculation. The thermodynamic properties of the fixed-volume solid are estimated using phonon energies, which depend on the frequencies and the lattice internal energy from DFT calculation at 0 K. The Gibbs free energy at pressure p, temperature T and volume V is given by $G(V,T) = U_L(V) + U_V(V, T) - TS(V, T) + pV$, where $U_v(V,T)$ and $S(V, T)$ represent the vibrational internal energy and vibrational entropy due to phonon contributions, respectively. The expressions for U_v and S are given as follows[51],

$$U_v(V,T) = \sum_{\mathbf{q},j} \hbar\omega_{\mathbf{q},j} \left[\frac{1}{2} + \frac{1}{\exp\left[\frac{\hbar\omega_{\mathbf{q},j}}{k_B T}\right]-1}\right] \quad (1)$$

$$S(V,T) = -k_B \sum_{\mathbf{q},j} \log\left[1 - \exp\left(-\hbar\omega_{\mathbf{q},j}/k_B T\right)\right] - \frac{1}{T}\sum_{\mathbf{q},j} \frac{\hbar\omega_{\mathbf{q},j}}{\exp\left[\hbar\omega_{\mathbf{q},j}/k_B T\right]-1} \quad (2)$$

where $\omega_{\mathbf{q},j}$ represents the phonon frequency at the wave vector $\mathbf{q}$ and band index j. The dependence on volume is omitted for simplicity. k_B and $\hbar$ refer to the Boltzmann constant and the reduced Planck constant, respectively.

To efficiently obtain the vibrational contributions to the entropy, phonon calculations were performed using a highly accurate M3GNet GIP fitted from a dataset of 5,595 r^{2}SCAN calculations. Then, we calculated the Helmholtz free energies for each compound in the Na-B-H phase diagram at 300 K and 650 K. The phonon thermodynamic properties were computed using the fitted Na-B-H GIP.

Machine learning interatomic potential and molecular dynamic simulations. The r^{2}SCAN relaxed bulk materials cubic-$NaBH_4$ (12 atoms), monoclinic-$Na_2B_{12}H_{12}$ (52 atoms), and o-NBH (128 atoms) were replicated by 4×4×4, 4×2×2, 2×2×2 so that all lattice parameters were larger than 10 Å. MD simulations were performed for 1 ns using pre-trained M3GNet potential at temperatures ranging from 300 K to 800 K, starting with 25 K increments from 300 K to 500 K, followed by 50 K increments up to 600 K, and then increasing by 100 K from 600 K to 800 K. The simulation utilized the NPT ensembles with a timestep of 1 fs. All MD simulations were carried out with LAMMPS. The visualization of trajectories was achieved by OVITO. The diffusivities were extracted from the MD trajectories by using the pymatgen-analysis-diffusion package[52,53].

The diffusion coefficient (D) of Na^+ ions was determined by applying a linear fit to the mean square displacement (MSD) versus time (t) using the Einstein–Smoluchowski equation as follows:

$$D = \frac{\langle[\vec{r}(t+\tau)-\vec{r}(t)]^2\rangle}{2dt} \quad (3)$$

Where $\vec{r}(t)$ is the position of the atom at the time t, τ is the time interval between atom positions $\vec{r}(t+\tau)$ and $\vec{r}(t)$. The MSD is computed by $[\vec{r}(t+\tau)-\vec{r}(t)]^2$. Therefore, the ionic conductivity is determined by the Nernst–Einstein equation:

$$\sigma(T) = {n(Ze)^2 D(T)}\Big/{k_B T} \quad (4)$$

Where n represents the Na atom density, e is the elementary charge, Z denotes the Li-ion charge, k_B is Boltzmann's constant, and T is the absolute temperature. Activation energies (E_a) were further determined by generating the Arrhenius plots.

The rotation speeds of $B_{12}H_{12}^{2-}$ and BH_4^- anions are artificially manipulated by proportionally increasing the cluster atomic mass. The rotation speed of each anion is determined as follows:

$$v_{rot} = \frac{\sum_0^{n_{atom}} \|[\vec{r}(t+\tau)-\vec{r}(t)-\Delta\mathrm{com}\|}{n_{atom}R} \quad (5)$$

Where $\vec{r}(t)$ is the position of the atom at the time t, τ is the time interval between atom positions $\vec{r}(t+\tau)$ and $\vec{r}(t)$. Δcom is the difference in the center-of-mass position between the time steps, the Euclidean norm $\|\bullet\|$ computes the distance, n_{atom} represents the total number of atoms and R denotes the radius of the anions.

Estimating the active Na^+ ions in the o-NBH is conducted by tracing the 96 Na^+ ions in the structure during the simulation. Based on the equation 3 and 4 relationship, the average Na^+ MSD to achieve the 18.39 mS cm^{-1} at 300 K is estimated to be around 21 $Å^2$. We also noted that the MSD of H, which exhibits only rotational but no long-ranged translational motion, is around 18 $Å^2$. Thus, we have adopted a more moderate cut-off of 21 $Å^2$ as the minimum MSD required for a Na^+ to be considered "active". The number of active Na^+ is then normalized by 96 Na^+ that are simulated in the calculation.

References

36 Cooper, S. J., Bertei, A., Shearing, P. R., Kilner, J. A. & Brandon, N. P. TauFactor: An open-source application for calculating tortuosity factors from tomographic data. *SoftwareX* **5**, 203-210, doi:10.1016/j.softx.2016.09.002 (2016).

37 Clark, S. J. *et al.* First principles methods using CASTEP. *Zeitschrift für Kristallographie - Crystalline Materials* **220**, 567-570, doi:10.1524/zkri.220.5.567.65075 (2005).

38 Perdew, J. P., Burke, K. & Ernzerhof, M. Generalized Gradient Approximation Made Simple. *Phys Rev Lett* **77**, 3865-3868, doi:10.1103/PhysRevLett.77.3865 (1996).

39 Monkhorst, H. J. & Pack, J. D. Special points for Brillouin-zone integrations. *Physical Review B* **13**, 5188-5192, doi:10.1103/PhysRevB.13.5188 (1976).

40 Liu, D. C. & Nocedal, J. On the limited memory BFGS method for large scale optimization. *Mathematical Programming* **45**, 503-528, doi:doi.org/10.1007/BF01589116 (1989).

41 Pickard, C. J. & Mauri, F. All-electron magnetic response with pseudopotentials: NMR chemical shifts. *Physical Review B* **63**, doi:10.1103/PhysRevB.63.245101 (2001).
42 Yates, J. R., Pickard, C. J. & Mauri, F. Calculation of NMR chemical shifts for extended systems using ultrasoft pseudopotentials. *Physical Review B* **76**, doi:10.1103/PhysRevB.76.024401 (2007).
43 Profeta, M., Mauri, F. & Pickard, C. J. Accurate first principles prediction of ^{17}O NMR parameters in SiO_2: assignment of the zeolite ferrierite spectrum. *J Am Chem Soc* **125**, 541-548, doi:https://doi.org/10.1021/ja027124r (2003).
44 Chen, C. & Ong, S. P. A universal graph deep learning interatomic potential for the periodic table. *Nat Comput Sci* **2**, 718-728, doi:10.1038/s43588-022-00349-3 (2022).
45 Zagorac, D., Muller, H., Ruehl, S., Zagorac, J. & Rehme, S. Recent developments in the Inorganic Crystal Structure Database: theoretical crystal structure data and related features. *J Appl Crystallogr* **52**, 918-925, doi:10.1107/S160057671900997X (2019).
46 Jain, A. *et al.* Commentary: The Materials Project: A materials genome approach to accelerating materials innovation. *APL Materials* **1**, doi:10.1063/1.4812323 (2013).
47 Qi, J., Ko, T. W., Wood, B. C., Pham, T. A. & Ong, S. P. Robust training of machine learning interatomic potentials with dimensionality reduction and stratified sampling. *npj Computational Materials* **10**, doi:10.1038/s41524-024-01227-4 (2024).
48 Bartok, A. P. & Yates, J. R. Regularized SCAN functional. *J Chem Phys* **150**, 161101, doi:10.1063/1.5094646 (2019).
49 Plimpton, S. Fast Parallel Algorithms for Short-Range Molecular Dynamics. *Journal of Computational Physics* **117**, 1-19, doi:10.1006/jcph.1995.1039

(1995).
50 Kresse, G. & Furthmuller, J. Efficient iterative schemes for ab initio total-energy calculations using a plane-wave basis set. *Phys Rev B Condens Matter* **54**, 11169-11186, doi:10.1103/PhysRevB.54.11169 (1996).
51 Togo, A. & Tanaka, I. First principles phonon calculations in materials science. *Scripta Materialia* **108**, 1-5, doi:10.1016/j.scriptamat.2015.07.021 (2015).
52 Deng, Z., Zhu, Z., Chu, I.-H. & Ong, S. P. Data-Driven First-Principles Methods for the Study and Design of Alkali Superionic Conductors. *Chemistry of Materials* **29**, 281-288, doi:10.1021/acs.chemmater.6b02648 (2016).
53 Ong, S. P. *et al.* Python Materials Genomics (pymatgen): A robust, open-source python library for materials analysis. *Computational Materials Science* **68**, 314-319, doi:10.1016/j.commatsci.2012.10.028 (2013).

Acknowledgment
The synchrotron radiation experiments were performed at Taiwan Photon Source (TPS), National Synchrotron Radiation Research Center (NSRRC). Electron microscopy was performed at the San Diego Nanotechnology Infrastructure (SDNI) of UCSD, a member of the National Nanotechnology Coordinated Infrastructure, which is supported by the National Science Foundation (Grant No.: ECCS-2025752). J.A.S. Oh is thankful for post-doctorate fellowship support from the Agency of Science, Technology, and Research (A*STAR).

Funding

The work at UC San Diego was supported by National Science Foundation through the Partnerships for Innovation (PFI) (grant no.: 2044465) and Shell Global Solutions Inc. (contract no. CW649697) and the work at Chicago was supported by Energy Storage Research Alliance (DE-AC02-06CH11357), an Energy Innovation Hub funded by the U.S. Department

of Energy, Office of Science, Basic Energy Sciences. The work in A*STAR was supported by A*STAR AME Programmatic Grant (ref. no.: A20H3b0140).

Competing interests

One provisional patent has been filed by University of California, San Diego Office of Innovation and Commercialization based on this work.

Authors contributions

J.A.S. Oh: Conceptualization, discovery and synthesis, analysis and investigation, and writing – initial draft; Z. Yu: computational calculation; C.-J Huang, P. Ridley, and B.J. Hwang: crystal structure characterization; C.-J Huang: tomography reconstruction and analysis; T. Zhang: DFT simulation and analysis of ss-NMR spectra. K.J. Griffith: Methodology, validation, supervision, and writing – initial draft. S.P. Ong: Methodology, validation, and supervision. S.Y. Meng: Conceptualization, fund acquisition, and supervision. All authors have provided written consent for the manuscript.

Data availability

All the data presented in this work are fully available from the corresponding authors.

Code availability

The DFT calculations input were generated by Pymatgen and being calculated by Vienna Ab initio Simulation Package (VASP). The Na-B-H machine learning interatomic potential was trained by M3GNet that was included in Materials Graph Library (matgl, https://github.com/materialsvirtuallab/matgl). The MLIP-MD simulation was carried out by the interface of matgl and lammps (https://github.com/advancesoftcorp/lammps). The diffusion analysis was conducted using pymatgen-analysis-diffusion package (https://github.com/materialsvirtuallab/pymatgen-analysis-diffusion).